



Publication Year	2020
Acceptance in OA	2025-02-20T09:50:41Z
Title	ARES I: WASP-76 b, A Tale of Two HST Spectra
Authors	GUILLEY, Gloria
Publisher's version (DOI)	10.3847/1538-3881/ab9225
Handle	http://hdl.handle.net/20.500.12386/36084
Journal	THE ASTRONOMICAL JOURNAL
Volume	160



ARES I: WASP-76 b, A Tale of Two HST Spectra*

Billy Edwards¹, Quentin Changeat¹, Robin Baeyens², Angelos Tsiraras¹, Ahmed Al-Refaei¹, Jake Taylor³, Kai Hou Yip¹, Michelle Fabienne Bieger⁴, Doriann Blain⁵, Amélie Gressier^{5,6,7}, Gloria Guilluy^{8,9}, Adam Yassin Jaziri¹⁰, Flavien Kiefer⁷, Darius Modirrousta-Galian^{11,12}, Mario Morvan¹, Lorenzo V. Mugnai¹³, William Pluriel¹⁰, Mathilde Poveda^{14,15}, Nour Skaf^{1,5}, Niall Whiteford^{16,17}, Sam Wright¹, Tiziano Zingales¹⁰, Benjamin Charnay⁵, Pierre Drossart⁵, Jérémy Lecote¹⁰, Olivia Venot¹⁴, Ingo Waldmann¹, and Jean-Philippe Beaulieu^{7,18}

¹ Department of Physics and Astronomy, University College London, London, UK; billy.edwards.16@ucl.ac.uk

² Instituut voor Sterrenkunde, KU Leuven, Celestijnenlaan 200D bus 2401, B-3001 Leuven, Belgium

³ Department of Physics (Atmospheric, Oceanic and Planetary Physics), University of Oxford, Parks Rd, Oxford, UK

⁴ College of Engineering, Mathematics and Physical Sciences, University of Exeter, North Park Road, Exeter, UK

⁵ LESIA Observatoire de Paris, Section de Meudon 5, place Jules Janssen F-92195 Meudon, France

⁶ LATMOS, CNRS, Sorbonne Université UVSQ, 11 boulevard d'Alembert, F-78280 Guyancourt, France

⁷ Sorbonne Universités, UPMC Université Paris 6 et CNRS, UMR 7095, Institut d'Astrophysique de Paris, Paris, France

⁸ Dipartimento di Fisica, Università degli Studi di Torino, via Pietro Giuria 1, I-10125 Torino, Italy

⁹ INAF Osservatorio Astrofisico di Torino, Via Osservatorio 20, I-10025 Pino Torinese, Italy

¹⁰ Laboratoire d'astrophysique de Bordeaux, Univ. Bordeaux, CNRS, B18N, allée Geoffroy Saint-Hilaire, F-33615 Pessac, France

¹¹ INAF Osservatorio Astronomico di Palermo, Piazza del Parlamento 1, I-90134 Palermo, Italy

¹² University of Palermo, Department of Physics and Chemistry, Via Archirafi 36, Palermo, Italy

¹³ La Sapienza Università di Roma, Department of Physics, Piazzale Aldo Moro 2, I-00185 Roma, Italy

¹⁴ Laboratoire Interuniversitaire des Systèmes Atmosphériques (LISA), UMR CNRS 7583, Université Paris-Est-Créteil, Université de Paris, Institut Pierre Simon Laplace, Créteil, France

¹⁵ Maison de la Simulation, CEA, CNRS, Univ. Paris-Sud, UVSQ, Université Paris-Saclay, F-91191 Gif-sur-Yvette, France

¹⁶ Institute for Astronomy, University of Edinburgh, Blackford Hill, Edinburgh EH9 3HJ, UK

¹⁷ Centre for Exoplanet Science, University of Edinburgh, Edinburgh EH9 3FD, UK

¹⁸ School of Physical Sciences, University of Tasmania, Private Bag 37 Hobart, Tasmania 7001, Australia

Received 2020 February 28; revised 2020 May 4; accepted 2020 May 8; published 2020 June 9

Abstract

We analyze the transmission and emission spectra of the ultra-hot Jupiter WASP-76 b, observed with the G141 grism of the Hubble Space Telescope's (HST) Wide Field Camera 3 (WFC3). We reduce and fit the raw data for each observation using the open-source software *Iraclis* before performing a fully Bayesian retrieval using the publicly available analysis suite *TauREx 3*. Previous studies of the WFC3 transmission spectra of WASP-76 b found hints of titanium oxide (TiO) and vanadium oxide (VO) or non-gray clouds. Accounting for a fainter stellar companion to WASP-76, we reanalyze this data and show that removing the effects of this background star changes the slope of the spectrum, resulting in these visible absorbers no longer being detected, eliminating the need for a non-gray cloud model to adequately fit the data but maintaining the strong water feature previously seen. However, our analysis of the emission spectrum suggests the presence of TiO and an atmospheric thermal inversion, along with a significant amount of water. Given the brightness of the host star and the size of the atmospheric features, WASP-76 b is an excellent target for further characterization with HST, or with future facilities, to better understand the nature of its atmosphere, to confirm the presence of TiO and to search for other optical absorbers.

Unified Astronomy Thesaurus concepts: [Exoplanet atmospheres \(487\)](#); [Exoplanet atmospheric composition \(2021\)](#); [Hubble Space Telescope \(761\)](#)

1. Introduction

Ultra-hot Jupiters are an intriguing population of exoplanets. With dayside temperatures greater than ~ 2000 K, these planets were truly unexpected and continue to unveil surprising traits. Despite being a rare outcome of planetary formation, many have been found using ground-based surveys such as the Wide Angle Search for Planets (WASP, Pollacco et al. 2006), the Hungarian Automated Telescope network (HAT, Bakos et al. 2013) and Kilodegree Extremely Little Telescope (KELT, Pepper et al. 2007). Given their size and temperature, as well as the brightness of their host stars, these planets are excellent targets for atmospheric characterization. Moreover, they offer the opportunity to explore atmospheric chemistry and dynamics in extreme conditions. Understanding their composition, and

thus their metallicity and carbon to oxygen ratio, is crucial for constraining formation and migration theories (Venturini et al. 2016; Madhusudhan et al. 2017).

The Wide Field Camera 3 (WFC3) onboard the Hubble Space Telescope (HST) has, along with Spitzer's InfraRed Array Camera (IRAC), been at the forefront of characterizing these planets. These very hot atmospheres were predicted to have inverted temperature–pressure profiles due to strong optical absorption by TiO and VO (Hubeny et al. 2003; Fortney et al. 2008). HST observations of two cooler hot Jupiters ($T < 2000$ K) detected non-inverted temperature profiles for WASP-43 b (Stevenson et al. 2014b) and HD 209458b (Line et al. 2016), which are consistent with the theoretical predictions of Fortney et al. (2008). However, observations of the emission spectra of ultra-hot Jupiters have, thus far, been inconclusive on their thermal structure and composition. While some have shown features due to water or optical absorbers, others are consistent with a simple blackbody fit

* ARES: Ariel Retrieval of Exoplanets School.

(e.g., Madhusudhan et al. 2011; Haynes et al. 2015; Evans et al. 2016, 2017, 2018; Beatty et al. 2017; Arcangeli et al. 2018; Kreidberg et al. 2018; Bourrier et al. 2020; Mikal-Evans et al. 2019). This variety may well be because the emission spectrum in this bandpass is dependent on both the water content and the thermal structure of the planet, and the G141 grism (1.1–1.7 μm) probes a region of the atmosphere where the temperature only varies slowly with pressure (Mansfield et al. 2018; Parmentier et al. 2018).

Upon the discovery of a companion, WASP-76 became the brightest star known to host a planet with a radius greater than 1.5 R_J (West et al. 2016). While brighter targets have since been discovered, WASP-76 b is still one of the best currently known targets for atmospheric characterization and the transmission spectrum was observed by the HST in 2015 November. The observations were taken with the WFC3 using the G141 grism which covers 1.1–1.7 μm . This spectrum was analyzed by Tsiaras et al. (2018) as part of a population study of 30 gaseous exoplanets. Retrievals by Tsiaras et al. (2018) suggested a water-rich atmosphere ($\log(\text{H}_2\text{O}) = -2.7 \pm 1.07$) with a 4.4σ detection of TiO and VO. However, as noted in the study, the abundances of TiO retrieved were likely to be nonphysical and affected by correlations between the molecular abundances, planet radius, and cloud pressure.

Retrieval analysis of this spectrum was also performed by Fisher & Heng (2018), who extracted a water abundance which was incompatible with the previous study ($\log(\text{H}_2\text{O}) = -5.3 \pm 0.61$). Fisher & Heng (2018) did not fit for TiO or VO but instead used a non-gray cloud model to explain the opacity seen at shorter wavelengths. WASP-76 b was one of two planets from their study of 38 transmission spectra that was not well fitted using the standard gray cloud model.

High-resolution ground-based observations offer the opportunity to resolve the spectral lines of exoplanet atmospheres and the High Accuracy Radial velocity Planet Searcher (Pepe et al. 2000) was used to analyze WASP-76 b and find evidence for absorption due to sodium (Seidel et al. 2019; Žák et al. 2019). Recent work by von Essen et al. (2020) using transmission data from Hubble’s Space Telescope Imaging Spectrograph (STIS) confirmed the presence of sodium and provided marginal evidence of titanium hydride (TiH).

Two transits of WASP-76 b were observed using the Echelle Spectrograph for Rocky Exoplanets and Stable Spectroscopic Observations instrument on the Very Large Telescope (VLT) and used to reveal an asymmetric absorption signature which was attributed to neutral iron (Fe, Ehrenreich et al. 2020). The signature was blueshifted on the trailing limb, proving evidence for strong day-to-night winds and an asymmetric dayside. However, the lack of signal on the leading limb means little Fe is present there and thus must be condensing on the nightside.

Here we present an analysis of the transmission and emission spectra of WASP-76 b, taken with the WFC3 G141 grism aboard HST. Although not reported in the discovery paper (West et al. 2016), the presence of a stellar companion was noted in several studies (Wöllert & Brandner 2015; Ginski et al. 2016; Ngo et al. 2016; Bohn et al. 2020) and the common proper motion of the two objects was confirmed by Southworth et al. (2020). This was not accounted for in previous WFC3 transmission studies and, using Wayne simulations (Varley et al. 2017), we show that this companion affects the spectral data obtained. We use Wayne to remove the contamination of the companion and reanalyze the transmission spectrum finding

evidence for H_2O but, while we were able to place upper limits on the TiO, VO, and FeH abundances, we were unable to well constrain other molecules. In the emission spectrum, we find indications of the presence of H_2O and TiO, along with a thermal inversion. Additionally we place upper limits on the abundances of FeH and VO.

2. Data Analysis

2.1. Data Reduction

Our analysis started from the raw spatially scanned spectroscopic images which were obtained from the Mikulski Archive for Space Telescopes.¹⁹ The transmission spectrum was acquired as part of proposal 14260, taken in 2015 November, while the observation of the eclipse was taken during proposal 14767 in 2016 November. We used Iraclis,²⁰ a specialized, open-source software for the analysis of WFC3 scanning observations (Tsiaras et al. 2016b) and the reduction process included the following steps: zero-read subtraction, reference pixels correction, nonlinearity correction, dark current subtraction, gain conversion, sky background subtraction, calibration, flat-field correction, and corrections for bad pixels and cosmic rays. For a detailed description of these steps, we refer the reader to the original Iraclis paper (Tsiaras et al. 2016b).

The reduced spatially scanned spectroscopic images were then used to extract the white (from 1.1 to 1.7 μm) and spectral light curves. The spectral light-curve bands were selected such that the SNR is approximately uniform across the planetary spectrum. We then discarded the first orbit of each visit as they present stronger wavelength-dependent ramps, and the first exposure after each buffer dump as these contain significantly lower counts than subsequent exposures (e.g., Deming et al. 2013; Tsiaras et al. 2016b; Mansfield et al. 2018). Additionally, for the third orbit of the transit, two further scans were removed to increase the quality of the fit (e.g., Kreidberg et al. 2018). For the fitting of the white light curves, the only free parameters were the mid-transit time and planet-to-star ratio. Alexoudi et al. (2018) showed that the inclination can have a strong effect on the derived slope of optical transmission data. We therefore checked that our results were not affected in this way by running light-curve fittings with the inclination as a free parameter. The spectral transit depths from these fittings did not differ from the fixed inclination case. However, the best-fit inclinations differed between the transit and eclipse light curve and so the orbital parameters were set to values from Ehrenreich et al. (2020). The limb-darkening coefficients were selected from the best available stellar parameters using values from Claret et al. (2012, 2013) and using the stellar parameters from Ehrenreich et al. (2020). We did not fit for the limb-darkening coefficients, as they are degenerate with other parameters, particularly given the periodic gaps in the HST data. Tsiaras et al. (2018) showed that fitting the limb-darkening coefficients does not generally affect the recovered spectrum and Morello et al. (2017) showed that uncertainties in stellar models do not significantly affect the atmospheric spectra in the WFC3 spectral band. The fitted white light curves for both observations are shown in Figure 1 while the spectral light curves are plotted in Figures 2 and 3.

¹⁹ <https://archive.stsci.edu/hst/>

²⁰ <https://github.com/ucl-exoplanets/Iraclis>

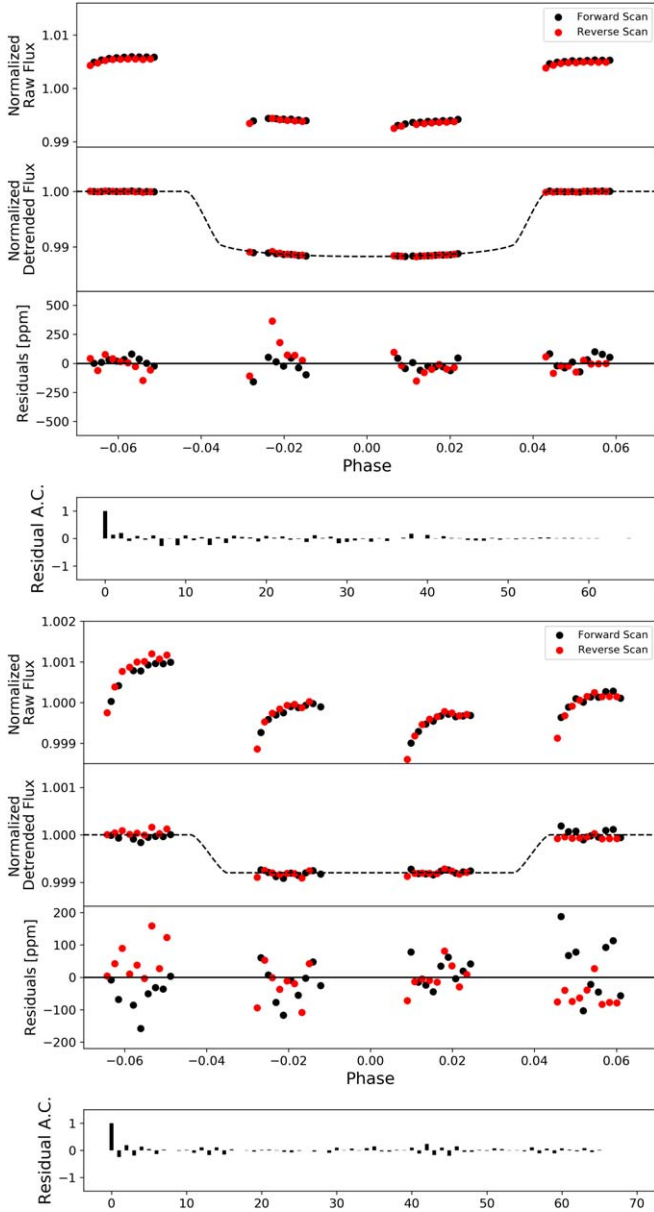


Figure 1. White light curves for the transmission (top) and emission (bottom) observations of WASP-76 b. First panel: raw light curve, after normalization. Second panel: light curve, divided by the best-fit model for the systematics. Third panel: residuals for best-fit model. Fourth panel: autocorrelation function of the residuals.

2.2. Removal of Companion Contamination

The stellar companion of WASP-76, reported by Bohn et al. (2020) and Southworth et al. (2020) has a K magnitude which is ~ 2.30 fainter and the separation between both stars is only $0''.436$. As such, it is expected to have contaminated the transmission and emission spectra obtained by Hubble. For exoplanet spectroscopy, this third light modifies the transit/eclipse depth. For the Hubble STIS observations analyzed by von Essen et al. (2020), the point spread functions of WASP-76 and its companion could be distinguished. However, due to the plate scale of HST WFC3, it is not resolvable in this case. Hence, to account for this, we used the freely available WFC3 simulator Wayne.²¹

Wayne is capable of producing grism spectroscopic frames, both in staring and in spatial scanning modes (Varley et al. 2017). Using the stellar parameters from Bohn et al. (2020), we utilized Wayne to model the contribution of the companion star to the spectral data obtained. We created simulated detector images of both the main and companion star, using these to extract the flux contribution in each spectral bin of each star. The correction to the spectra is then applied as a wavelength-dependent dilution factor which is derived as a ratio of extracted flux between the stars. Such an approach has previously been used on WFC3 data (e.g., for WASP-12 b Stevenson et al. 2014a; Kreidberg et al. 2015; Tsiaras et al. 2018). The recovered transmission and emission spectra, before and after the correction was applied, are shown in Figure 4 along with the correction factor used. Two trends are seen: first, the transit and eclipse depths are increased and, second, the slope of the spectrum is changed in each case due to the differing spectral types of the stars.

2.3. Atmospheric Modeling

The retrieval of the transmission and emission spectrum were performed using the publicly available retrieval suite TauREx 3 (Al-Refaie et al. 2019).²² For the star parameters and the planet mass, we used the values from Ehrenreich et al. (2020) listed in Table 1. In our runs, we assumed that WASP-76 b possesses a primary atmosphere with a ratio $\text{H}_2/\text{He} = 0.17$. To this we added trace gases and included the molecular opacities from the ExoMol (Tennyson et al. 2016), HITRAN (Gordon et al. 2016), and HITEMP (Gordon et al. 2017) databases for H_2O (Polyansky et al. 2018), CH_4 (Yurchenko & Tennyson 2014), CO (Li et al. 2015), CO_2 (Rothman et al. 2010), FeH (Dulick et al. 2003; Wende et al. 2010), TiO (McKemmish et al. 2019), VO (McKemmish et al. 2016), and H^- . On top of this, we also included Collision-Induced Absorption (CIA) from $\text{H}_2\text{--H}_2$ (Abel et al. 2011; Fletcher et al. 2018) and $\text{H}_2\text{--He}$ (Abel et al. 2012) as well as Rayleigh scattering for all molecules.

For the H^- opacity, we used the description in John (1988). The bound-free absorption coefficient ($k^{\text{bf}}(\lambda, T)$) corresponds to the photodetachment of an electron by hydrogen ion and the free-free absorption coefficient ($k^{\text{ff}}(\lambda, T)$) results from the interaction of free electrons in the field of neutral hydrogen atoms. These coefficients (in $\text{cm}^4 \text{ dyne}^{-1}$) are expressed per unit electron pressure and per hydrogen atom. One can calculate the electron partial pressure in dyne cm^{-2} ($P_{e-}(\text{dyne cm}^{-2})$) using:

$$P_{e-}(\text{dyne cm}^{-2}) = P(\text{bar}) \times V_{e-} \times 10^6, \quad (1)$$

where P (bar) is the atmospheric pressure in bar and V_{e-} is the volume mixing ratio of electrons. The weighted cross section σ_{H^-} for the H^- absorption is given by:

$$\sigma_{\text{H}^-}(\lambda, T) = (k^{\text{bf}}(\lambda, T) + k^{\text{ff}}(\lambda, T)) \times P_{e-}(\text{dyne cm}^{-2}) * V_{\text{H}}, \quad (2)$$

where V_{H} is the volume mixing ratio of neutral hydrogen atoms. Hence we are left with two free parameters: the electron and neutral hydrogen volume mixing ratios. In our retrieval analysis, we fixed the hydrogen volume mixing ratio and imposed a profile inspired from Parmentier et al. (2018). We used the two-layer model from Changeat et al. (2019) to describe the increasing abundance of neutral hydrogen atoms with altitude. We chose a

²¹ <https://github.com/ucl-exoplanets/wayne>

²² https://github.com/ucl-exoplanets/TauREx3_public

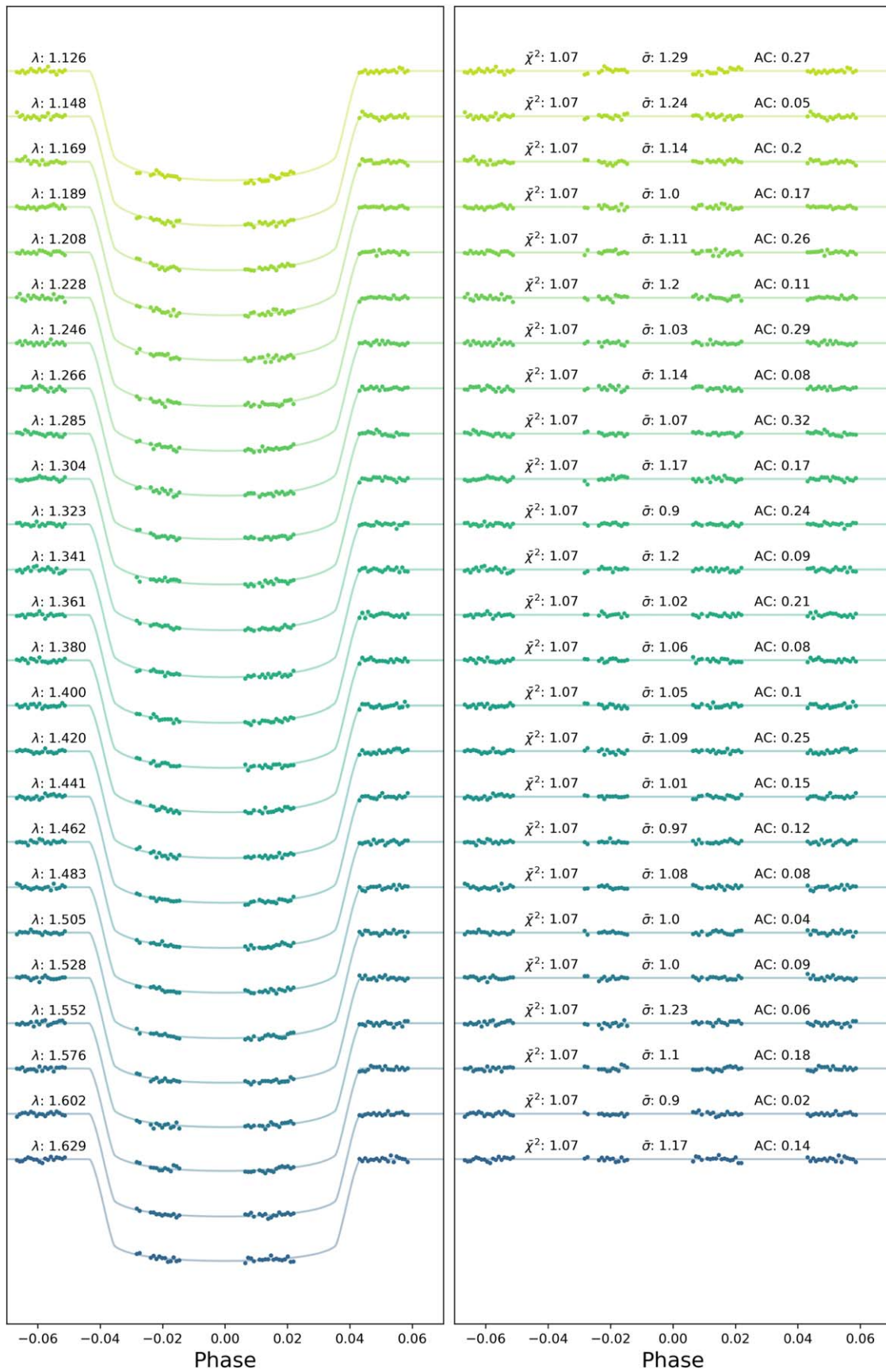


Figure 2. Spectral light curves fitted with Iraclis for the transmission spectra where, for clarity, an offset has been applied. Left: the detrended spectral light curves with best-fit model plotted. Right: residuals from the fitting with values for the chi-squared (χ^2), the standard deviation of the residuals with respect to the photon noise (σ), and the autocorrelation (AC).

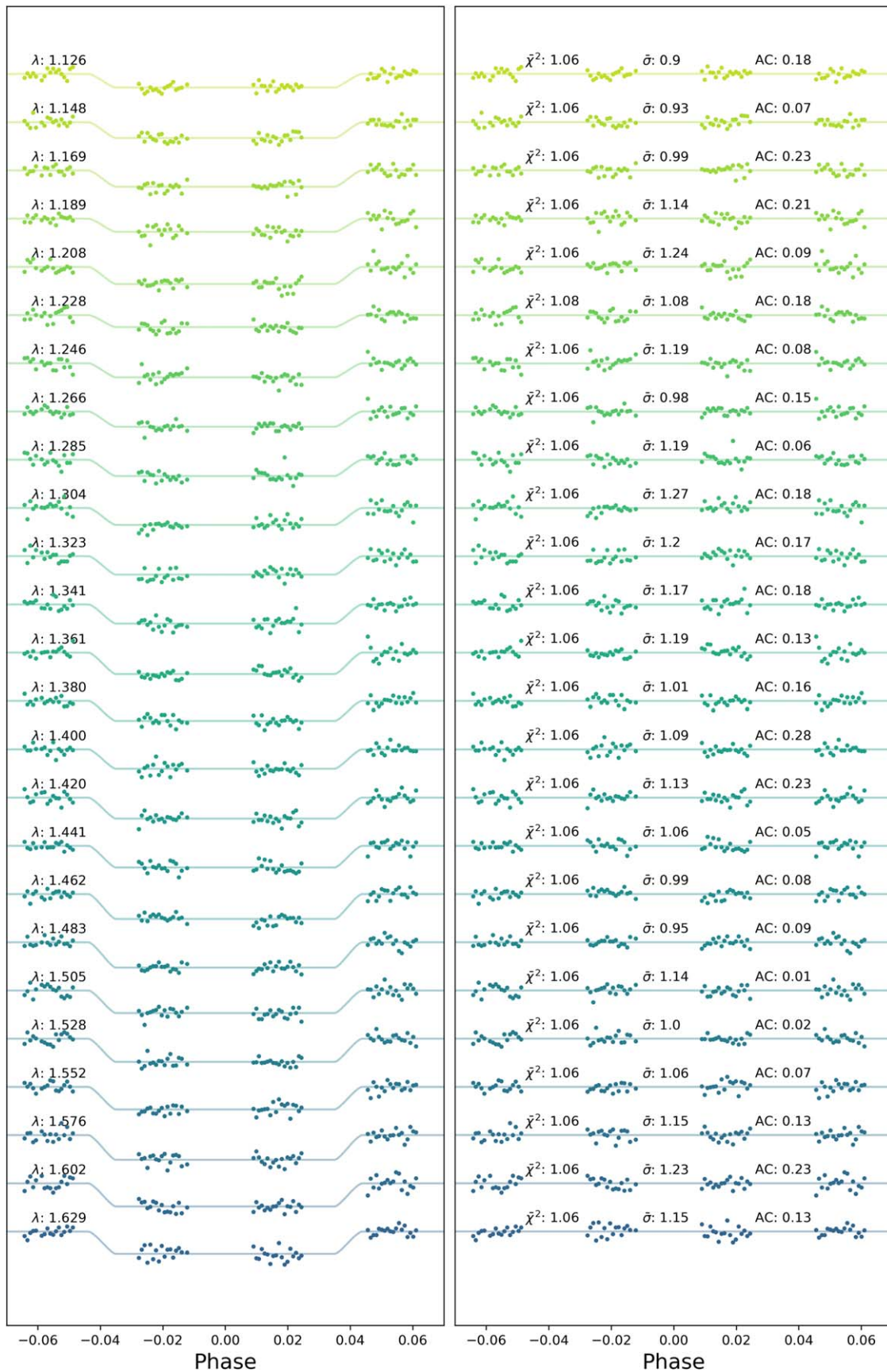


Figure 3. Spectral light curves fitted with Iraclis for the emission spectra where, for clarity, an offset has been applied. Left: the detrended spectral light curves with best-fit model plotted. Right: residuals from the fitting with values for the chi-squared (χ^2), the standard deviation of the residuals with respect to the photon noise (σ), and the autocorrelation (AC).

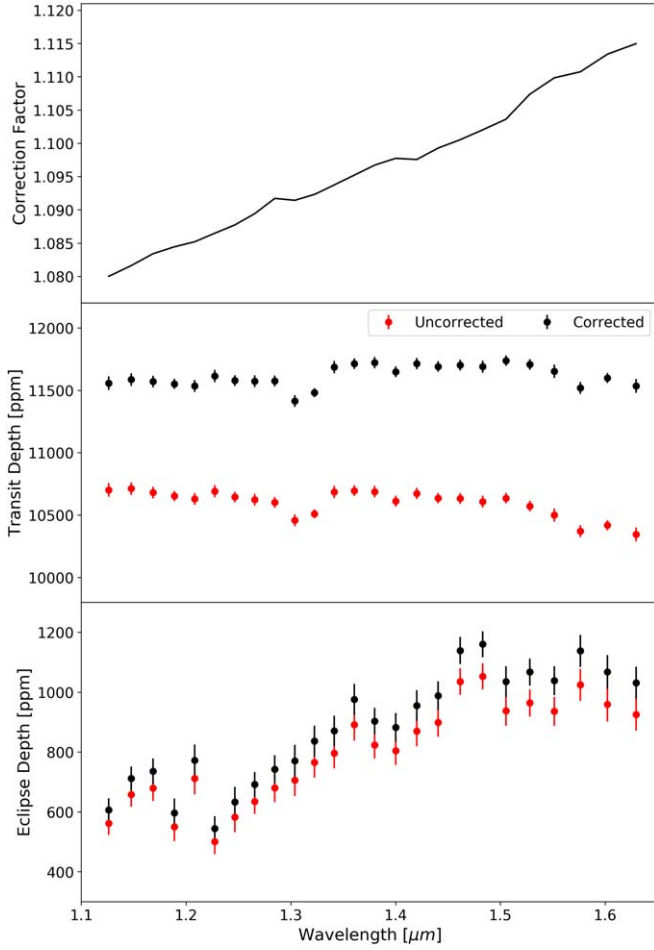


Figure 4. Top: wavelength-dependent correction factor derived from the Wayne simulations. Middle: the corrected (black) and uncorrected (red) transmission spectra. Bottom: the same but for the emission spectra.

surface abundance of 10^{-2} , a top abundance of 0.5 and a layer pressure change at 10^{-1} bar. Therefore, the only remaining parameter to constrain the H^- absorption is the electron volume mixing ratio V_{e^-} .

Since, in emission spectroscopy, the radius is degenerate with temperature (e.g., Griffith 2014), we fixed its value to the best-fit value from the transmission retrieval. In transmission, we assumed an isothermal atmosphere while, for the emission, we used a non-physically informed approach consisting of three temperature points. This led to five free variables: surface temperature (T_{surf}), temperature of point 1 (T_1), temperature of point 2 (T_{top}), pressure of point 1 (P_1), and pressure of point at the top (P_{top}). These points were allowed to vary freely in the pressure grid ranging from 10 to 10^{-10} bar. In our retrieval analysis, we used uniform priors for all parameters as described in Table 2. Finally, we explored the parameter space using the nested sampling algorithm Multinest (Feroz et al. 2009) with 750 live points and an evidence tolerance of 0.5.

3. Results

The recovered transmission and emission spectra are given in Table 3. The analysis of the transmission spectra by Tsiaras et al. (2018) detected water along with the suggestion of TiO and VO. Having accounted for the stellar companion, the slope at the blue end of the spectrum is reduced and thus our retrieval

Table 1
Stellar and Planetary Parameters for WASP-76 b Used during the Iraclis, Wayne, and TauREx Analyses

Input Stellar and Planetary Parameters*	
T_* (K)	6329 ± 65
R_* (R_\odot)	1.756 ± 0.071
M_* (M_\odot)	1.458 ± 0.021
$\log_{10}(g)$ (cm s^{-2})	4.196 ± 0.106
[Fe/H]	0.366 ± 0.053
a/R_*	$4.08^{+0.02}_{-0.06}$
e	0 (fixed)
i	$89.623^{+0.005}_{-0.034}$
ω	0 (fixed)
P (days)	$1.80988198^{+0.00000064}_{-0.00000056}$
T_0 (BJD _{TDB})	$2458080.626165^{+0.000418}_{-0.000367}$
M_p	$0.894^{+0.014}_{-0.013}$
R_p	$1.854^{+0.077}_{-0.076}$

*Taken from Ehrenreich et al. (2020)

Companion Star Parameters	
T_* (K)	4824^\dagger
R_* (R_\odot)	0.83^\dagger
M_* (M_\odot)	0.79^\dagger
$\log_{10}(g)$ (cm s^{-2})	4.5^\ddagger
[Fe/H]	0.0^\ddagger

† Taken or derived from Bohn et al. (2020)

‡ Assumed value

Table 2
List of the Retrieved Parameters, their Uniform Prior Bounds, the Scaling Used and the Retrieved Value

Transmission			
Parameters	Prior Bounds	Scale	Retrieved
H_2O	-12; -2	log	$-2.85^{+0.42}_{-0.71}$
CH_4	-12; -2	log	unconstrained
CO	-12; -2	log	unconstrained
CO_2	-12; -2	log	unconstrained
TiO	-12; -2	log	< -6.1
VO	-12; -2	log	< -6.9
FeH	-12; -2	log	< -7.3
e^-	-12; -2	log	unconstrained
T_{term} (K)	1600; 4000	linear	2231^{+265}_{-283}
P_{clouds} (Pa)	6; -2	log	$0.91^{+0.70}_{-0.46}$
R_p (R_{jup})	1.3; 2.2	linear	$1.67^{+0.04}_{-0.03}$
Emission			
Parameters	Prior Bounds	Scale	Retrieved
H_2O	-12; -2	log	$-2.81^{+0.51}_{-0.65}$
CH_4	-12; -2	log	unconstrained
CO	-12; -2	log	unconstrained
CO_2	-12; -2	log	unconstrained
TiO	-12; -2	log	$-5.62^{+0.71}_{-1.57}$
VO	-12; -2	log	< -7.9
FeH	-12; -2	log	< -7.0
e^-	-12; -2	log	unconstrained
T_{surf} (K)	1600; 4000	linear	2805^{+689}_{-680}
T_1 (K)	1600; 4000	linear	2413^{+147}_{-159}
T_{top} (K)	1600; 4000	linear	3147^{+189}_{-168}
P_1 (Pa)	6; 2	log	$4.50^{+0.89}_{-1.13}$
P_{top} (Pa)	3; -2	log	$-0.20^{+1.36}_{-1.10}$

Table 3Corrected Transmission and Emission Spectra Derived Here Along with the Chi-squared (χ^2), the Standard Deviation of the Residuals with Respect to the Photon Noise ($\bar{\sigma}$), and the Autocorrelation (AC) for the Spectral Light-Curve Fits

Wavelength (μm)	Bandwidth (μm)	Correction Factor	Transit				Eclipse			
			Depth (%)	χ^2	$\bar{\sigma}$	AC	Depth (%)	χ^2	$\bar{\sigma}$	AC
1.12625	0.0219	1.080007	1.1557 \pm 0.0054	1.07	1.29	0.27	0.0607 \pm 0.0039	1.06	0.90	0.18
1.14775	0.0211	1.081612	1.1585 \pm 0.0052	1.07	1.24	0.05	0.0711 \pm 0.0040	1.06	0.93	0.07
1.16860	0.0206	1.083408	1.1570 \pm 0.0047	1.07	1.14	0.20	0.0736 \pm 0.0043	1.06	0.99	0.23
1.18880	0.0198	1.084441	1.1551 \pm 0.0041	1.07	1.00	0.17	0.0597 \pm 0.0048	1.06	1.14	0.21
1.20835	0.0193	1.085204	1.1534 \pm 0.0048	1.07	1.11	0.26	0.0772 \pm 0.0053	1.06	1.24	0.09
1.22750	0.0190	1.086487	1.1614 \pm 0.0050	1.07	1.20	0.11	0.0544 \pm 0.0041	1.08	1.08	0.18
1.24645	0.0189	1.087721	1.1578 \pm 0.0042	1.07	1.03	0.29	0.0633 \pm 0.0050	1.06	1.19	0.08
1.26550	0.0192	1.089421	1.1572 \pm 0.0047	1.07	1.14	0.08	0.0692 \pm 0.0042	1.06	0.98	0.15
1.28475	0.0193	1.091716	1.1574 \pm 0.0044	1.07	1.07	0.32	0.0742 \pm 0.0047	1.06	1.19	0.06
1.30380	0.0188	1.091428	1.1414 \pm 0.0048	1.07	1.17	0.17	0.0770 \pm 0.0053	1.06	1.27	0.18
1.32260	0.0188	1.092315	1.1480 \pm 0.0036	1.07	0.90	0.24	0.0836 \pm 0.0052	1.06	1.20	0.17
1.34145	0.0189	1.093736	1.1686 \pm 0.0050	1.07	1.20	0.09	0.0870 \pm 0.0050	1.06	1.17	0.18
1.36050	0.0192	1.095211	1.1713 \pm 0.0043	1.07	1.02	0.21	0.0976 \pm 0.0052	1.06	1.19	0.13
1.38005	0.0199	1.096720	1.1721 \pm 0.0046	1.07	1.06	0.08	0.0903 \pm 0.0044	1.06	1.01	0.16
1.40000	0.0200	1.097740	1.1649 \pm 0.0044	1.07	1.05	0.10	0.0882 \pm 0.0048	1.06	1.09	0.28
1.42015	0.0203	1.097564	1.1714 \pm 0.0046	1.07	1.09	0.25	0.0955 \pm 0.0051	1.06	1.13	0.23
1.44060	0.0206	1.099283	1.1691 \pm 0.0042	1.07	1.01	0.15	0.0988 \pm 0.0048	1.06	1.06	0.05
1.46150	0.0212	1.100529	1.1701 \pm 0.0043	1.07	0.97	0.12	0.1139 \pm 0.0045	1.06	0.99	0.08
1.48310	0.0220	1.102016	1.1689 \pm 0.0048	1.07	1.08	0.08	0.1160 \pm 0.0044	1.06	0.95	0.09
1.50530	0.0224	1.103614	1.1737 \pm 0.0042	1.07	1.00	0.04	0.1035 \pm 0.0051	1.06	1.14	0.01
1.52800	0.0230	1.107372	1.1707 \pm 0.0042	1.07	1.00	0.09	0.1067 \pm 0.0045	1.06	1.00	0.02
1.55155	0.0241	1.109843	1.1652 \pm 0.0054	1.07	1.23	0.06	0.1038 \pm 0.0048	1.06	1.06	0.07
1.57625	0.0253	1.110741	1.1518 \pm 0.0048	1.07	1.10	0.18	0.1138 \pm 0.0053	1.06	1.15	0.13
1.60210	0.0264	1.113385	1.1598 \pm 0.0040	1.07	0.90	0.02	0.1067 \pm 0.0056	1.06	1.23	0.23
1.62945	0.0283	1.114973	1.1535 \pm 0.0056	1.07	1.17	0.14	0.1031 \pm 0.0054	1.06	1.15	0.13

Note. Note that the correction factor has already been applied to the transit and eclipse depths.

does not find substantial evidence of significant abundances of TiO or VO. However, the recovered water abundance of $\log(\text{H}_2\text{O}) = -2.85^{+0.47}_{-0.71}$ is consistent with that from Tsiaras et al. (2018) ($\log(\text{H}_2\text{O}) = -2.70 \pm 1.07$). While we did attempt to retrieve the carbon-based molecules, CO, CO₂, and CH₄, we were unable to constrain their abundance as they lack strong features in the G141 wavelength range. Additionally, the abundance of e⁻ (H⁻ opacity) was not constrained but we could place a 1 σ upper limit of $\log(\text{FeH}) < -7.3$. Our best-fit model favors the presence of clouds at $\log(P) = 0.91$ Pa but we note there is significant correlation with the abundance of water. The best-fit spectrum and the posteriors are given in Figure 5 while the priors and results from the retrieval are given in Table 2. To understand the statistical significance of our results, we also ran a “molecule free” retrieval where the only fitted parameters were the planet radius, planet temperature, and cloud-top pressure. Scattering due to Rayleigh and CIA were also included. The difference in Bayesian log evidence was computed to be 24.7 in favor of the fit including molecules, providing significant evidence of the detection of molecular features ($>7\sigma$, Kass & Raftery 1995). This is equivalent to the Atmospheric Detectability Index as defined in Tsiaras et al. (2018).

Our retrieval analysis of the emission spectrum of WASP-76 b finds significant evidence of TiO, with an abundance of $\log(\text{TiO}) = -5.62^{+0.71}_{-1.57}$, along with H₂O at a concentration of $\log(\text{H}_2\text{O}) = -2.81^{+0.51}_{-0.65}$. Additionally the emission spectrum places an upper bound on the presence of both iron hydride and vanadium oxide at $\log(\text{FeH}), \log(\text{VO}) \approx -7$. Again, the carbon-based molecules were not constrained since there is a lack of spectral information in the WFC3 G141 wavelength band. Due to

the presence of optical absorbers, our analysis suggests a temperature inversion in the dayside of WASP-76 b. The retrieval posteriors for the emission spectrum are shown in Figure 6 while Figure 7 displays the best-fit temperature profiles for both observations. Here the model was compared to a simple blackbody fit, which converged to $T_{\text{BB}} = 2778 \pm 8$ K. The difference in Bayesian log evidence was 12.4, signifying the fit with H₂O, TiO, and a thermal inversion is statistically preferable at $>5\sigma$.

4. Discussion

4.1. Comparison to Chemical Models

To provide context to our findings, we compare the results of our retrieval analysis to a self-consistent forward model computed with petitCODE, a 1D numerical iterator solving for radiative-convective and chemical equilibrium (Mollière et al. 2015, 2017). The code includes radiative scattering, opacities for H₂, H⁻, H₂O, CO, CO₂, CH₄, HCN, H₂S, NH₃, OH, C₂H₂, PH₃, SiO, FeH, Na, K, Fe, Fe⁺, Mg, Mg⁺, TiO, and VO, as well as collision-induced absorption by H₂-H₂ and H₂-He. Cloud condensation of refractory species is included in the equilibrium chemistry, but no cloud opacities are considered in this simulation. Our petitCODE model for WASP-76 b was computed using the stellar and planetary parameters determined by West et al. (2016). An intrinsic temperature of 600 K was adopted for this inflated planet, following the prescription by Thorngren et al. (2019). A global planetary averaged redistribution of the irradiation was assumed.

Two models were produced: one with, and one without, the presence of TiO and VO. For the former case, the resulting temperature–pressure profile and equilibrium abundances are

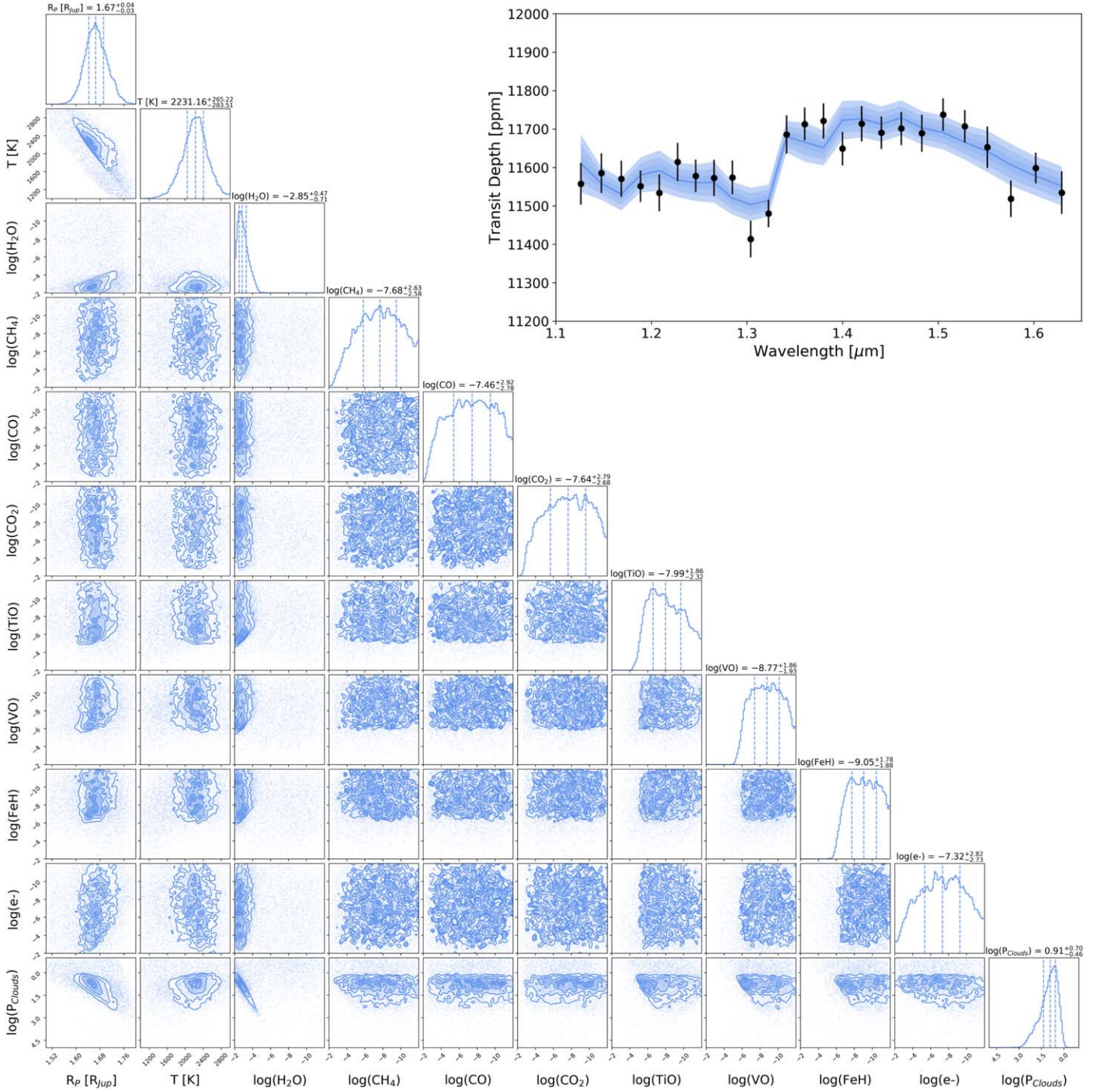


Figure 5. Posterior distributions for the transmission spectrum of WASP-76 b which suggest the presence of a large amount of H_2O as well as placing upper limits on the abundances of TiO, VO, and FeH. Inset: transmission spectrum (black) with best-fit model and $1-3\sigma$ uncertainties (blue).

shown in Figure 7. The temperature profile shows an inversion in the range probed by transmission/emission spectroscopy (typically ~ 1 mbar to ~ 100 mbar) and this was only present for the model with TiO/VO opacities. A similar result is shown in Lothringer et al. (2018), who found the same dichotomy between atmospheres with and without TiO/VO for planets with equilibrium temperatures of $T_{\text{eq}} = 2250$ K.

Our retrieval emission abundance for TiO ($\log(\text{TiO}) = -5.62^{+0.71}_{-1.57}$) is consistent to 1σ with the $\log(\text{TiO}) \approx -7$ predicted by petitCODE and the upper boundary of $\log(\text{FeH}) < 7$ that was retrieved from the emission spectrum also

agrees well with the self-consistent petitCODE model. In transmission, the upper limit placed on these molecules is greater than the predicted abundances and thus the non-detection is likely due to the quality of the data. Furthermore, the extent of H_2O in the terminator and on the dayside is also similar to the abundance predicted with the chemical equilibrium model. Finally, the VO chemical profile is seen to be below the sensitivity of the emission spectrum. This is due to TiO, FeH, and VO possessing similar features in the G141 wave band. This degeneracy may also affect the TiO abundance retrieved.

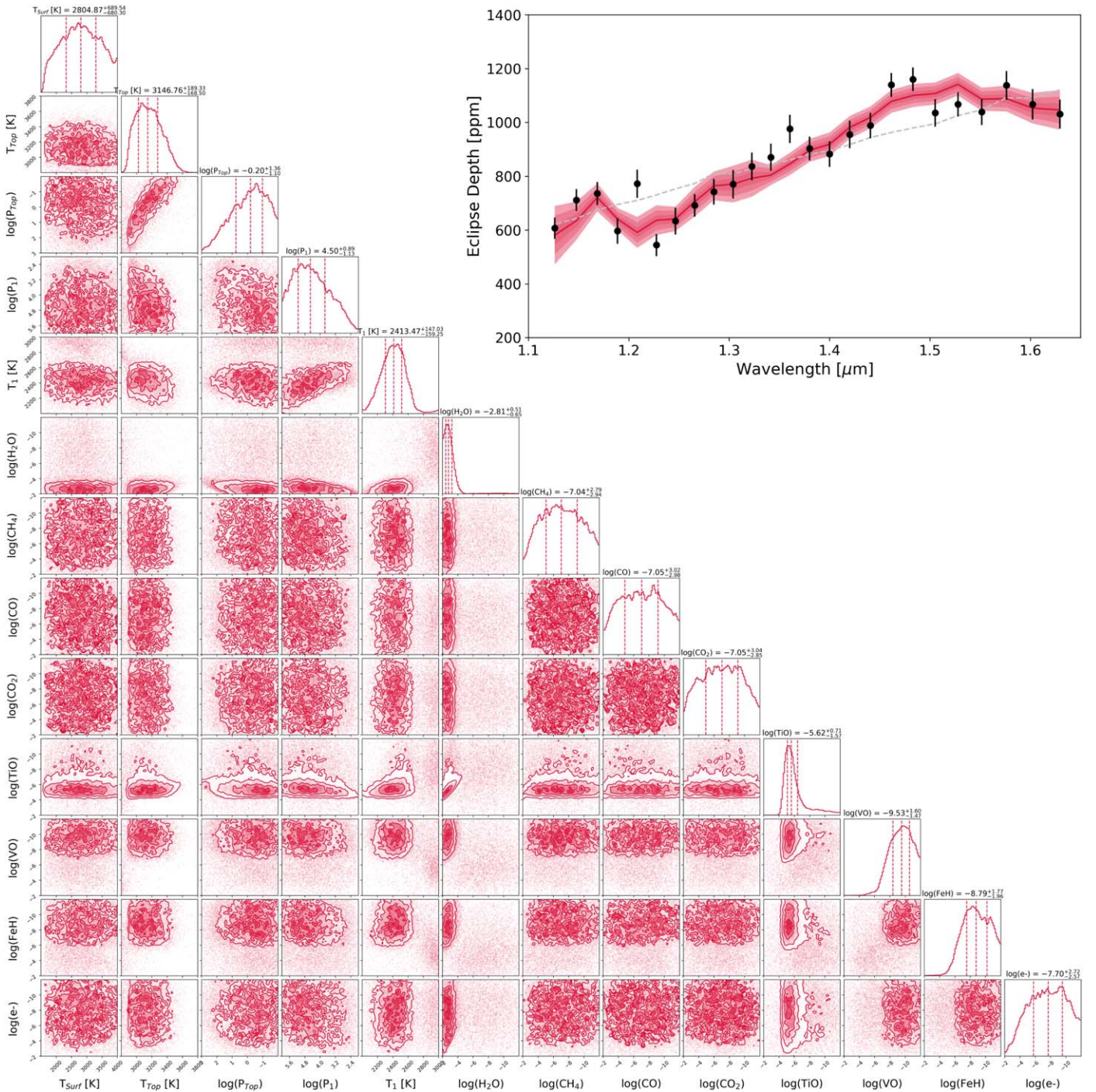


Figure 6. Posterior distributions for the emission spectrum of WASP-76 b, which suggest the presence of a large amount of H₂O as well as TiO. Inset: emission spectrum (black) with best-fit model and 1-3 σ uncertainties (red). Also shown is a blackbody fit (gray), which has a temperature of $T_{\text{BB}} = 2778 \pm 8$ K.

The equilibrium chemical abundances of most molecules, except CO, drop significantly for pressures lower than a few mbar due to thermal dissociation in the upper atmosphere (Arcangeli et al. 2018; Lothringer et al. 2018; Parmentier et al. 2018). Models by Parmentier et al. (2018) suggest that, for WASP-76 b, nearly half the water should be dissociated at the 1.4 μm photosphere. Thus the H₂O bands are significantly muted due to thermal dissociation in the upper layers of the atmosphere, owing to the intense irradiation by the nearby host star, as seen in Arcangeli et al. (2018), Lothringer et al. (2018), and Kreidberg et al. (2018). Between 1 and 1.4 μm , both water

and TiO/VO opacities are low, leading to a region where H⁻, TiO, and H₂O opacities have similar strength. Particularly, H⁻ opacity fills the gap between the two water bands at 1.1 and 1.4 μm , effectively lowering the contrast between the top and the bottom of the bands.

From Figure 7, we also note that the quick depletion of molecules in the atmosphere may introduce inaccuracies in the retrieval, as it assumes a single chemical abundance for the whole atmospheric pressure range. However, the chemical abundances of most molecules remain roughly constant for the pressure range that can be probed with our observations. Here,

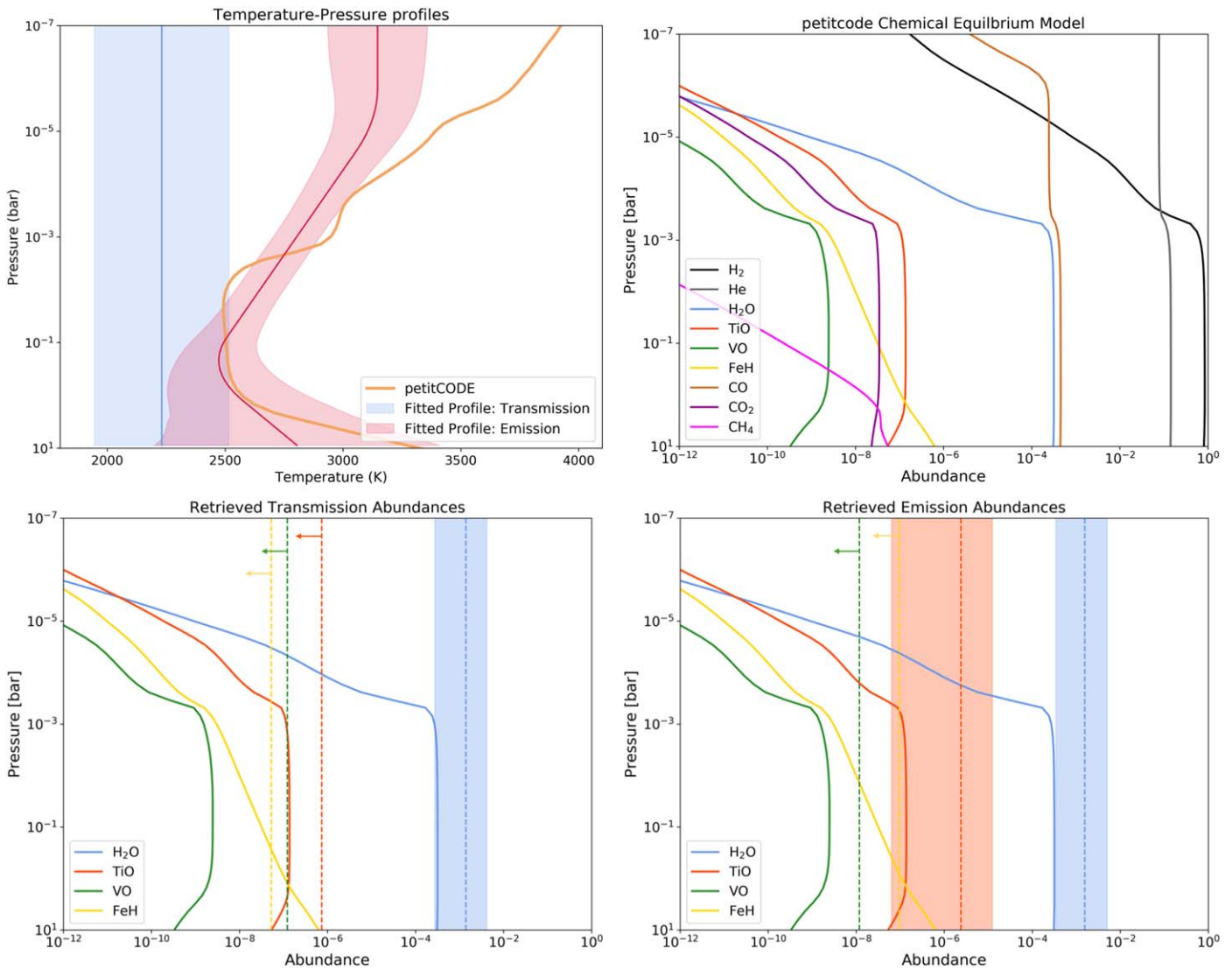


Figure 7. Results of our self-consistent petitCODE model for WASP-76 b and our retrievals on WFC3 data. Top left: comparison of the temperature–pressure profiles. The petitCODE model (orange) features a thermal inversion at 1 mbar, due to absorption by TiO and VO, and closely matches the retrieved profile. Top right: molecular abundances for the petitCODE simulation. The equilibrium fractions of most molecules (*bottom*) remain approximately constant for pressures higher than a few mbar. They drop quickly at lower atmospheric pressures due to thermal dissociation. Bottom left: comparison of constrained molecular abundances in transmission (dotted lines) to those from the petitCODE simulation (solid lines). The water abundance is seen to be around 1σ higher than predicted. Bottom right: comparison of constrained molecular abundances in emission to those from the petitCODE simulation. Again the water abundance is seen to be around 1σ higher than predicted while the TiO concentration is within 1σ of the model.

our isochemical retrievals suggest a thermal inversion which would be attributed to the absorption of TiO and VO at high altitudes. We could therefore expect the abundance of TiO and VO to differ significantly with pressure. However, the data quality is unlikely to support a retrieval with such complexity due to the narrow wavelength coverage but such complexities will need to be accounted for in the analysis of data from the next generation of facilities (Changeat et al. 2019).

4.2. Previous Claims of Optical Absorbers

Optical absorbers have been proposed as one of the leading theories as to why ultra-hot Jupiters exhibit thermal inversions (e.g., Fortney et al. 2008). Hence, many atmospheric studies of these planets have been undertaken through both transmission and emission spectroscopy, with some planets studied through both methods.

WASP-19 b has been studied via transmission spectroscopy at near-infrared wavelengths with claims confirming and refuting the presence of TiO. The retrievals of the STIS G430L, G750L, WFC3 G141, and Spitzer IRAC observations suggest the presence of water at $\log(\text{H}_2\text{O}) \approx -4$ but show no evidence of optical absorbers (Sing et al. 2016; Barstow et al. 2017; Pinhas et al. 2019). However, ground-based transits acquired with the European Southern Observatory’s VLT, using the low-resolution FORS2 spectrograph ($R \sim 3000$) which covers the entire visible-wavelength domain (0.43–1.04 μm), suggested the presence of TiO, to a confidence level of 7.7σ (Sedaghati et al. 2017). However, Espinoza et al. (2019) found a featureless spectrum and argue the results of Sedaghati et al. (2017) are likely to be contaminated by stellar activity.

Evidence for a thermal inversion and optical absorbers has been seen of HAT-P-7 b, which was first studied in emission during the commissioning program of Kepler when the satellite

detected the eclipse as part of an optical phase curve (Borucki et al. 2009). This optical eclipse measurement was combined with Spitzer photometry over $3.5\text{--}8\ \mu\text{m}$ to infer the presence of a thermal inversion (Christiansen et al. 2010), which was suggested due to the high flux ratio in the $4.5\ \mu\text{m}$ channel of Spitzer compared to the $3.6\ \mu\text{m}$ channel. Their chemical equilibrium models associated these emission features with CO, H₂O, and CH₄. A thermal inversion was also reported to provide the best fit to these data by the atmospheric models of Spiegel & Burrows (2010) and Madhusudhan & Seager (2010). All three studies noted that models without a thermal inversion could also explain the data, though only with a very high abundance of CH₄. More recently, Mansfield et al. (2018) obtained two eclipses using the HST WFC3 G141 grism. When combined with previous observations, it was found to be best fit with a thermal inversion due to optical absorbers, but at a low statistical significance when compared to a simpler blackbody fit.

Finally, some planets have been observed with both transit and eclipse spectroscopy. For instance, studies of WASP-33 b have suggested the presence of aluminum oxide (AlO) in its transmission spectrum (von Essen et al. 2019) while the WFC3 emission is best fit by TiO and a thermal inversion (Haynes et al. 2015). Other studies using WFC3 G141 that have concluded optical absorbers may be present include WASP-121 b by Evans et al. (2017). WASP-121 b has an equilibrium temperature of 2500 K and H₂O was detected at a 5σ confidence with indications of absorption at high altitudes implying the presence of VO or TiO. The best-fit VO abundance was $\log(\text{VO}) = -3.5^{+0.4}_{-0.6}$. Subsequently, observations of WASP-121 b with the G102 grism were taken and combined with the original data. In this further study, H⁻ was included as an opacity source and the results were not consistent with the previously recovered VO abundance (Mikal-Evans et al. 2019). Bourrier et al. (2020) also performed a retrieval on the combined data, with the addition of data from TESS, and concluded VO abundance of $\log(\text{VO}) = -6.03^{+0.50}_{-0.69}$, far lower than the initial retrieval on WFC3 G141 data. Additionally, the optical phase curve presented in Daylan et al. (2019) suggested inefficient heat transport. This agrees with the work of Fortney et al. (2008), which postulated that the presence of optical absorbers would lead to, and require, large day-night temperature contrasts. However, Merritt et al. (2020) used high-resolution ground-based observations to place limits on the maximum abundances of TiO and VO in the terminator of WASP-121 b to $\log(\text{TiO}) < -9.26$ and $\log(\text{VO}) < -7.88$. Nevertheless the authors of this study note that these upper bounds are degenerate with the cloud deck and scattering properties while also being limited by the accuracy of the VO line lists. Thus, the presence of these optical absorbers cannot be definitively ruled out as yet.

Therefore, our analysis here makes WASP-76 b only the second ultra-hot Jupiter to be studied through both transmission and emission spectroscopy using WFC3 in scanning mode. In the analysis of WASP-121 b’s transmission and emission spectra by Evans et al. (2018), Mikal-Evans et al. (2019), chemical equilibrium models were used to fit the data. These suggested super-solar metallicities of 10–30 and 5–50 \times solar to 1σ in transmission and emission respectively. These metallicity ranges provide H₂O abundances which are similar to those recovered here (10^{-3} – 10^{-4}). The models from Parmentier et al. (2018) suggest that, for WASP-121 b, $\sim 70\%$ of the H₂O in the $1.4\ \mu\text{m}$ photosphere should be dissociated, compared to $\sim 50\%$

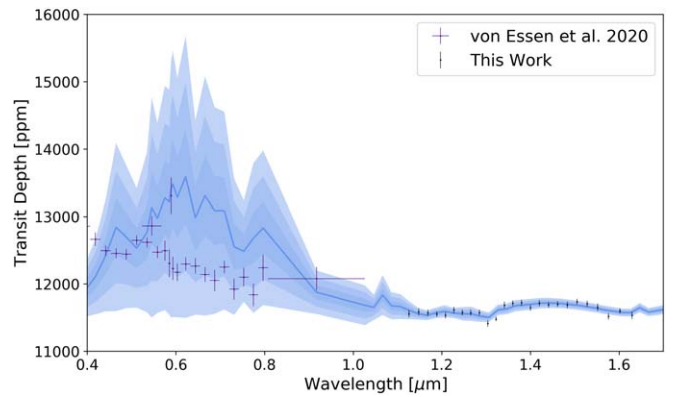


Figure 8. Comparison of the best-fit model to the WFC3 data and the STIS data from von Essen et al. (2020). Until a transmission spectrum is obtained with HST WFC3 G102 ($0.8\text{--}1.1\ \mu\text{m}$), which would provide continuous wavelength coverage between STIS and WFC3 G141, the compatibility of the data sets cannot be ascertained.

in WASP-76 b. Additionally, the metallicity (Fe/H) of WASP-76 is greater than that of WASP-121 and both are above solar, at 0.366 and 0.12 respectively (Ehrenreich et al. 2020; Mikal-Evans et al. 2019). We could therefore expect WASP-76 b to have slightly more H₂O than WASP-121 b but, while the best-fit solution agrees with this prediction, the 1σ errors on the abundance are too large to be conclusive.

4.3. Further Characterization of WASP-76 b

The atmosphere of WASP-76 b has been characterized in a number of other works. Notably, von Essen et al. (2020) used HST STIS to study the transmission spectrum of WASP-76 b. Hence, we extrapolated our best-fit model to the WFC3 data into the visible and over-plotted the data from von Essen et al. (2020). Figure 8 shows that, in the spectral region covered by STIS, our uncertainties are very large. This is due to the wide range of abundances that TiO, VO, and FeH could take, based on our analysis of WFC3 alone, and thus it is tempting to combine the data sets to reduce said uncertainty. However, without overlapping wavelength coverage, this is a dangerous pursuit at the best of times as the spectra could be offset due to the imperfect correction of instrument systematics, differing orbital parameters used in the fitting of the light curves, or temporal variations of the star–planet system. In this study, we have the additional complexity of the third-source contamination and differing methods in the removal of this stellar companion. For WASP-12 b, which also suffered this issue, Kreidberg et al. (2015) found the WFC3 data to be incompatible with that from STIS. Therefore we must, for now, resist the temptation to amalgamate data sets from multiple instruments. However, the addition of a transit observation with the G102 grism would provide continuous wavelength coverage from 0.3 to $1.7\ \mu\text{m}$, confirming the compatibility of the data and allowing the planet’s terminator to be studied in far greater detail.

The acquisition of a secondary eclipse observation of WASP-76 b with the G102 grism of WFC3, which would extend the wavelength coverage into the red optical where emission bands due to species such as TiO, VO, and FeH are more easily detectable, would further our knowledge of this planet and be valuable in providing additional evidence for, or refuting the presence of, TiO and in searching for other optical absorbers.

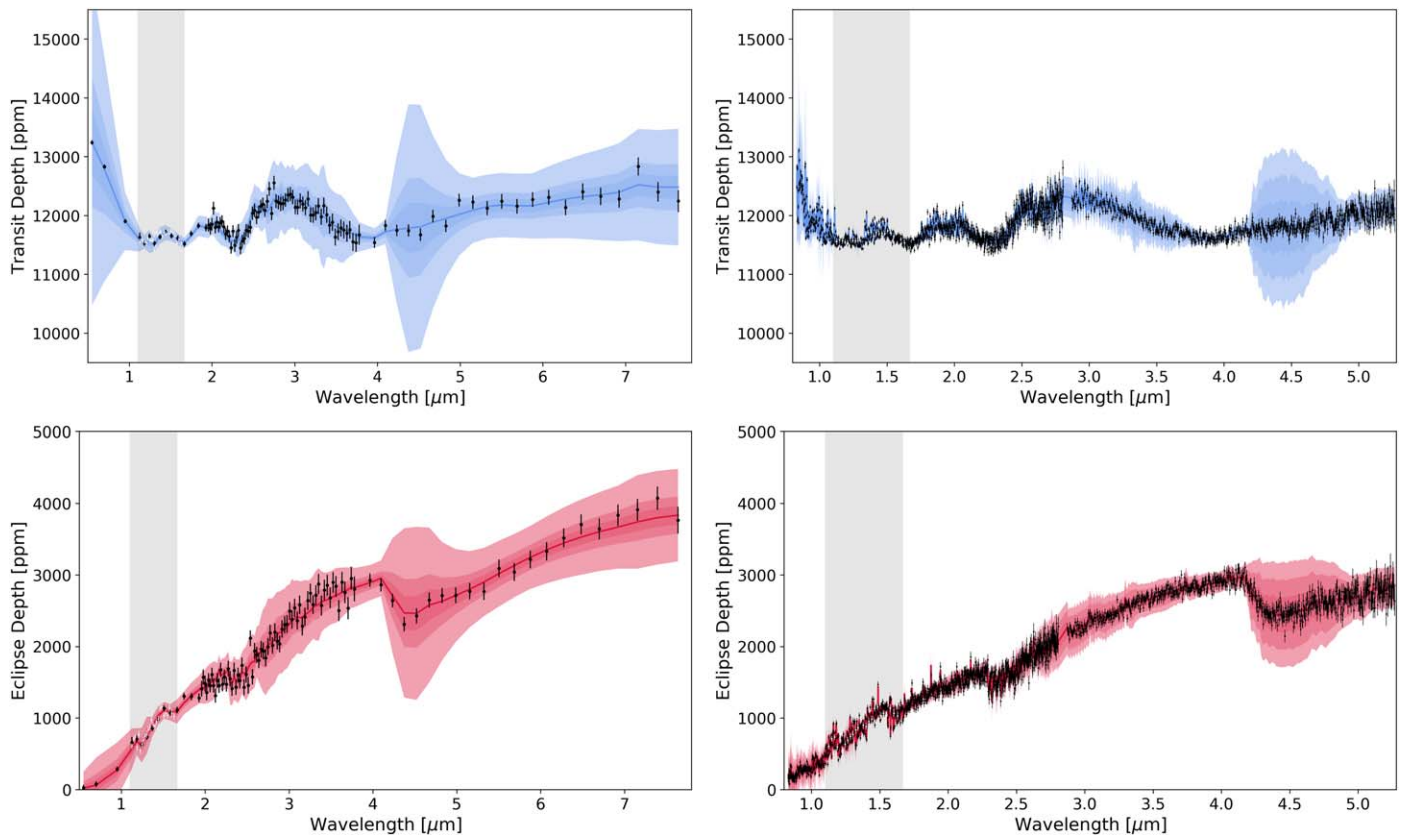


Figure 9. Simulated Ariel and JWST observations of the best-fit spectra from Hubble WFC3 observations. The Ariel spectra (left) are for a single observation at the native resolution of the instrumentation (i.e., Tier 3) while the JWST spectra (right) are for two observations, one using NIRISS G700XD and the second with NIRSpec G395M. The gray box indicates the wavelength range covered by the G141 grism and the data points from this study are shown in white. Note that, for all simulated observations, we have added Gaussian scatter.

Future space telescopes James Webb Space Telescope (JWST) (Greene et al. 2016), Twinkle (Edwards et al. 2019) and Ariel (Tinetti et al. 2018) will provide a far wider wavelength range. These missions will definitely move the exoplanet field from an era of detection into one of characterization, allowing for the identification of the molecular species present and their chemical profile, insights into the atmospheric temperature profile and the detection and characterization of clouds. Ariel, the ESA M4 mission due for launch in 2028, will conduct a survey of ~ 1000 planets to answer the question: how chemically diverse are the atmospheres of exoplanets? WASP-76 b is an excellent target for study with Ariel (Edwards et al. 2019), through both transmission and emission spectroscopy, and simulated error bars from L. Mugnai et al. (2020, in preparation) have been added to the best-fit spectra to showcase this in Figure 9. Additionally, ExoWebb (B. Edwards et al. 2020, in preparation) has been used to simulate the capability of JWST for studying this planet. For both facilities, the predicted error bars are far smaller than the 1σ uncertainty in the best-fit spectrum to the Hubble WFC3 data and thus they will allow for far tighter constraints on molecular constituents to be imposed.

5. Conclusions

Both the transmission and emission spectra of WASP-76 b, obtained by Hubble WFC3, have been analyzed. We have used open-source codes to reduce the data, remove contamination from a close stellar companion, and fit the final spectra. The transmission spectrum exhibits a large water feature while the dayside of the planet shows strong evidence for titanium oxide,

as well as water, and is best fit by an atmospheric thermal inversion. The abundances retrieved closely match those from chemical equilibrium models. However, further observations with Hubble, or future space-based facilities, will result in a better understanding of the chemical constituents of the atmosphere and help refine the models presented here.

This work was realized as part of ARES, the Ariel Retrieval Exoplanet School, in Biarritz in 2019 September. The school was organized by Jean-Philippe Beaulieu, Angelos Tsiraras and Ingo Waldmann with the financial support of CNES. This work is based on observations made with the NASA/ESA Hubble Space Telescope. These publicly available observations were taken as part of proposals 14260 and 14767, led by Drake Deming and David Sing respectively. These were obtained from the Hubble Archive which is part of the Mikulski Archive for Space Telescopes. We are thankful to those who operate this archive, the public nature of which increases scientific productivity and accessibility (Peek et al. 2019).

B.E., Q.C., M.M., A.T., and I.W. are funded through the ERC Consolidator grant ExoAI (GA 758892) and the STFC grants ST/P000282/1, ST/P002153/1, ST/S002634/1 and ST/T001836/1. R.B. is a Ph.D. fellow of the Research Foundation-Flanders (FWO). N.S. acknowledges the support of the IRIS-OCAV, PSL. M.P. acknowledges support by the European Research Council under Grant Agreement ATMO 757858 and by the CNES. W.P. and T.Z. have received funding from the European Research Council (ERC) under the European Union’s Horizon 2020 research and innovation program (grant agreement No. 679030/




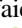



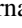


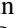

WHIPLASH). O.V. thanks the CNRS/INSU Programme National de Planétologie (PNP) and CNES for funding support. J.P.B. acknowledges the support of the University of Tasmania through the UTAS Foundation and the endowed Warren Chair in Astronomy, Rodolphe Cledassou, Pascale Danto and Michel Viso (CNES).

We are grateful to John Southworth for informing us on the presence, and the characteristics, of the stellar companion. We also thank Paul Mollière, for helpful comments and for providing the latest updates to petitCODE, and Karan Molaverdikhani for providing atomic and ion opacities for our petitCODE simulations.

Finally, we thank our anonymous referee for prompt, insightful comments which led to the improvement of the manuscript.

Software: Iraclis (Tsiaras et al. 2016b), TauREX 3 (Al-Refaie et al. 2019), Wayne (Varley et al. 2017), petitCODE (Mollière et al. 2015), pylightcurve (Tsiaras et al. 2016a), ExoTETHyS (Morello et al. 2020), ArielRad (L. Mugnai et al. 2020, in preparation), ExoWebb (B. Edwards et al. 2020, in preparation), Astropy (Astropy Collaboration et al. 2018), h5py (Collette 2013), emcee (Foreman-Mackey et al. 2013), Matplotlib (Hunter 2007), Multinest (Feroz et al. 2009), Pandas (McKinney 2011), Numpy (Oliphant 2006), SciPy (Virtanen et al. 2020).

ORCID iDs

Billy Edwards  <https://orcid.org/0000-0002-5494-3237>
 Quentin Changeat  <https://orcid.org/0000-0001-6516-4493>
 Angelos Tsiaras  <https://orcid.org/0000-0003-3840-1793>
 Ahmed Al-Refaie  <https://orcid.org/0000-0003-2241-5330>
 Mario Morvan  <https://orcid.org/0000-0001-8587-2112>
 Nour Skaf  <https://orcid.org/0000-0002-9372-5056>
 Tiziano Zingales  <https://orcid.org/0000-0001-6880-5356>
 Benjamin Charnay  <https://orcid.org/0000-0003-0977-6545>
 Jérémy Leconte  <https://orcid.org/0000-0002-3555-480X>
 Olivia Venot  <https://orcid.org/0000-0003-2854-765X>
 Ingo Waldmann  <https://orcid.org/0000-0002-4205-5267>
 Jean-Philippe Beaulieu  <https://orcid.org/0000-0003-0014-3354>

References

- Abel, M., Frommhold, L., Li, X., & Hunt, K. L. 2011, *JPCA*, 115, 6805
 Abel, M., Frommhold, L., Li, X., & Hunt, K. L. 2012, *JChPh*, 136, 044319
 Alexoudi, X., Mallonn, M., von Essen, C., et al. 2018, *A&A*, 620, A142
 Al-Refaie, A. F., Changeat, Q., Waldmann, I. P., & Tinetti, G. 2019, arXiv:1912.07759
 Arcangeli, J., Désert, J.-M., Line, M. R., et al. 2018, *ApJL*, 855, L30
 Astropy Collaboration, Price-Whelan, A. M., Sipőcz, B. M., et al. 2018, *AJ*, 156, 123
 Bakos, G. Á., Csabry, Z., Penev, K., et al. 2013, *PASP*, 125, 154
 Barstow, J. K., Aigrain, S., Irwin, P. G. J., & Sing, D. K. 2017, *ApJ*, 834, 50
 Beatty, T. G., Madhusudhan, N., Tsiaras, A., et al. 2017, *AJ*, 154, 158
 Bohn, A. J., Southworth, J., Ginski, C., et al. 2020, *A&A*, 635, A73
 Borucki, W. J., Koch, D., Jenkins, J., et al. 2009, *Sci*, 325, 709
 Bourrier, V., Kitzmann, D., Kuntzer, T., et al. 2020, *A&A*, 637, A36
 Changeat, Q., Edwards, B., Waldmann, I. P., & Tinetti, G. 2019, *ApJ*, 886, 39
 Christiansen, J. L., Ballard, S., Charbonneau, D., et al. 2010, *ApJ*, 710, 97
 Claret, A., Hauschildt, P. H., & Witte, S. 2012, *A&A*, 546, A14
 Claret, A., Hauschildt, P. H., & Witte, S. 2013, *A&A*, 552, A16
 Collette, A. 2013, Python and HDF5 (Sebastopol, CA: O'Reilly & Associates)
 Daylan, T., Günther, M. N., Mikal-Evans, T., et al. 2019, arXiv:1909.03000
 Deming, D., Wilkins, A., McCullough, P., et al. 2013, *ApJ*, 774, 95
 Dulick, M., Bauschlicher, C. W. J., Burrows, A., et al. 2003, *ApJ*, 594, 651
 Edwards, B., Mugnai, L., Tinetti, G., Pascale, E., & Sarkar, S. 2019, *AJ*, 157, 242
 Edwards, B., Rice, M., Zingales, T., et al. 2019, *ExA*, 47, 29
 Ehrenreich, D., Lovis, C., Allart, R., et al. 2020, *Natur*, 7805, 597
 Espinoza, N., Rackham, B. V., Jordán, A., et al. 2019, *MNRAS*, 482, 2065
 Evans, T. M., Sing, D. K., Goyal, J. M., et al. 2018, *AJ*, 156, 283
 Evans, T. M., Sing, D. K., Kataria, T., et al. 2017, *Natur*, 548, 58
 Evans, T. M., Sing, D. K., Wakeford, H. R., et al. 2016, *ApJL*, 822, L4
 Feroz, F., Hobson, M. P., & Bridges, M. 2009, *MNRAS*, 398, 1601
 Fisher, C., & Heng, K. 2018, *MNRAS*, 481, 4698
 Fletcher, L. N., Gustafsson, M., & Orton, G. S. 2018, *ApJS*, 235, 24
 Foreman-Mackey, D., Hogg, D. W., Lang, D., & Goodman, J. 2013, *PASP*, 125, 306
 Fortney, J. J., Lodders, K., Marley, M. S., & Freedman, R. S. 2008, *ApJ*, 678, 1419
 Ginski, C., Mugrauer, M., Seeliger, M., et al. 2016, *MNRAS*, 457, 2173
 Gordon, I. E., Rothman, L. S., Hill, C., et al. 2017, *JQSRT*, 203, 3
 Gordon, I., Rothman, L. S., Wilzewski, J. S., et al. 2016, AAS/DPS Meeting, 48, 421.13
 Greene, T. P., Line, M. R., Montero, C., et al. 2016, *ApJ*, 817, 17
 Griffith, C. A. 2014, *RSPTA*, 372, 20130086
 Haynes, K., Mandell, A. M., Madhusudhan, N., Deming, D., & Knutson, H. 2015, *ApJ*, 806, 146
 Hubeny, I., Burrows, A., & Sudarsky, D. 2003, *ApJ*, 594, 1011
 Hunter, J. D. 2007, *CSE*, 9, 90
 John, T. L. 1988, *A&A*, 193, 189
 Kass, R. E., & Raftery, A. E. 1995, *J. Am. Stat. Assoc.*, 90, 773
 Kreidberg, L., Line, M. R., Bean, J. L., et al. 2015, *ApJ*, 814, 66
 Kreidberg, L., Line, M. R., Parmentier, V., et al. 2018, *AJ*, 156, 17
 Li, G., Gordon, I. E., Rothman, L. S., et al. 2015, *ApJS*, 216, 15
 Line, M. R., Stevenson, K. B., Bean, J., et al. 2016, *AJ*, 152, 203
 Lothringer, J. D., Barman, T., & Koskinen, T. 2018, *ApJ*, 866, 27
 Madhusudhan, N., Bitsch, B., Johansen, A., & Eriksson, L. 2017, *MNRAS*, 469, 4102
 Madhusudhan, N., Harrington, J., Stevenson, K. B., et al. 2011, *Natur*, 469, 64
 Madhusudhan, N., & Seager, S. 2010, *ApJ*, 725, 261
 Mansfield, M., Bean, J. L., Line, M. R., et al. 2018, *AJ*, 156, 10
 McKemmish, L. K., Masseron, T., Hoeijmakers, H. J., et al. 2019, *MNRAS*, 488, 2836
 McKemmish, L. K., Yurchenko, S. N., & Tennyson, J. 2016, *MNRAS*, 463, 771
 McKinney, W. 2011, in Proc. 9th Python in Science Conf., ed. S. van der Walt & J. Millman (SciPy), 56
 Merritt, S. R., Gibson, N. P., Nugroho, S. K., et al. 2020, *A&A*, 636, A117
 Mikal-Evans, T., Sing, D. K., Goyal, J. M., et al. 2019, *MNRAS*, 488, 2222
 Mollière, P., van Boekel, R., Bouwman, J., et al. 2017, *A&A*, 600, A10
 Mollière, P., van Boekel, R., Dullemond, C., Henning, T., & Mordasini, C. 2015, *ApJ*, 813, 47
 Morello, G., Claret, A., Martin-Lagarde, M., et al. 2020, *AJ*, 159, 75
 Morello, G., Tsiaras, A., Howarth, I. D., & Homeier, D. 2017, *AJ*, 154, 111
 Ngo, H., Knutson, H. A., Hinkley, S., et al. 2016, *ApJ*, 827, 8
 Oliphant, T. E. 2006, A Guide to NumPy, Vol. 1 (Spanish Fork, UT: Trelgol Publishing)
 Parmentier, V., Line, M. R., Bean, J. L., et al. 2018, *A&A*, 617, A110
 Peek, J., Desai, V., White, R. L., et al. 2019, *BAAAS*, 51, 105
 Pepe, F., Mayor, M., Benz, W., et al. 2000, *Proc. SPIE*, 4008, 582
 Pepper, J., Pogge, R. W., DePoy, D. L., et al. 2007, *PASP*, 119, 923
 Pinhas, A., Madhusudhan, N., Gandhi, S., & MacDonald, R. 2019, *MNRAS*, 482, 1485
 Pollacco, D. L., Skillen, I., Collier Cameron, A., et al. 2006, *PASP*, 118, 1407
 Polyansky, O. L., Kyuberis, A. A., Zbov, N. F., et al. 2018, *MNRAS*, 480, 2597
 Rothman, L., Gordon, I., Barber, R., et al. 2010, *JQSRT*, 111, 2139
 Sedaghati, E., Boffin, H. M. J., MacDonald, R. J., et al. 2017, *Natur*, 549, 238
 Seidel, J. V., Ehrenreich, D., Wyttenbach, A., et al. 2019, *A&A*, 623, A166
 Sing, D. K., Fortney, J. J., Nikolov, N., et al. 2016, *Natur*, 529, 59
 Southworth, J., Bohn, A. J., Kenworthy, M. A., Ginski, C., & Mancini, L. 2020, *A&A*, 635, A74
 Spiegel, D. S., & Burrows, A. 2010, *ApJ*, 722, 871
 Stevenson, K. B., Bean, J. L., Seifahrt, A., et al. 2014a, *AJ*, 147, 161
 Stevenson, K. B., Désert, J.-M., Line, M. R., et al. 2014b, *Sci*, 346, 838
 Tennyson, J., Yurchenko, S. N., Al-Refaie, A. F., et al. 2016, *JMolSp*, 327, 73
 Thorngren, D., Gao, P., & Fortney, J. J. 2019, *ApJL*, 884, L6
 Tinetti, G., Drossart, P., Eccleston, P., et al. 2018, *ExA*, 46, 135
 Tsiaras, A., Waldmann, I., Rocchetto, M., et al. 2016a, pylightcurve: Exoplanet lightcurve model, Astrophysics Source Code Library, ascl:1612.018
 Tsiaras, A., Waldmann, I. P., Rocchetto, M., et al. 2016b, *ApJ*, 832, 202
 Tsiaras, A., Waldmann, I. P., Zingales, T., et al. 2018, *AJ*, 155, 156
 Varley, R., Tsiaras, A., & Karpouzias, K. 2017, *ApJS*, 231, 13

- Venturini, J., Alibert, Y., & Benz, W. 2016, [A&A](#), **596**, A90
- Virtanen, P., Gommers, R., Oliphant, T. E., et al. 2020, [Nat. Methods](#), **17**, 261
- von Essen, C., Mallonn, M., Hermansen, S., et al. 2020, [A&A](#), **637**, A76
- von Essen, C., Mallonn, M., Welbanks, L., et al. 2019, [A&A](#), **622**, A71
- Wende, S., Reiners, A., Seifahrt, A., & Bernath, P. F. 2010, [A&A](#), **523**, A58
- West, R. G., Hellier, C., Almenara, J. M., et al. 2016, [A&A](#), **585**, A126
- Wöllert, M., & Brandner, W. 2015, [A&A](#), **579**, A129
- Yurchenko, S. N., & Tennyson, J. 2014, [MNRAS](#), **440**, 1649
- Žák, J., Kabáth, P., Boffin, H. M. J., Ivanov, V. D., & Skarka, M. 2019, [AJ](#), **158**, 120